Single Nuclear Pores Visualized by Confocal Microscopy and Image Processing

Ulrich Kubitscheck, Peter Wedekind, Oliver Zeidler, Monika Grote, and Reiner Peters
Institut für Medizinische Physik und Biophysik, Westfälische Wilhelms-Universität, 48149 Münster, Germany

ABSTRACT How nuclear pore complexes, mediating the transport of nucleic acids, proteins, and metabolites between cell nucleus and cytoplasm, are arranged in the nuclear envelope is essentially unknown. Here we describe a method combining high-resolution confocal imaging with image processing and pattern recognition to visualize single nuclear pore complexes (120 nm diameter), determine their relative positions with nanometer accuracy, and analyze their distribution in situ. The method was tested by means of a model system in which the very same sample areas could be imaged by confocal and electron microscopy. It was thus found that single fluorescent beads of 105 nm nominal diameter could be localized with a lateral accuracy of <20 nm and an axial accuracy of ~20 nm. The method was applied to digitonin-permeabilized 3T3 cells, whose nuclear pore complexes were fluorescently labeled with the anti-nucleoporin antibody mAb414. Stacks of optical sections were generated by confocal imaging at high resolution. Herein the nuclear pore complexes appeared as bright diffraction-limited spots whose centers were localized by fitting them by three-dimensional gaussians. The nearest-neighbor distribution function and the pair correlation function were calculated and found to agree well with those of randomly distributed hard cylinders of 138 ± 17 nm diameter, but not with those of randomly distributed points or nonrandomly distributed cylinders. This was supported by a cluster analysis. Implications for the direct observation of the transport of single particles and molecules through individual nuclear pore complexes are discussed.

INTRODUCTION

The exchange of nucleic acids, proteins, and metabolites between nucleus and cytoplasm is mediated by the nuclear pore complex (NPC), an elaborate macromolecular assembly spanning the nuclear envelope (for a review, see Akey and Radermacher, 1993; Panté and Aebi, 1994; Hinshaw, 1994; Fabre and Hurt, 1994; Melchior and Gerace, 1995; Forbes and Johnson, 1995; Goldberg and Allen, 1995). The NPC probably consists of >100 different proteins, has a mass of ~125 MDa (Reichelt et al., 1990), and has an overall cylindrical shape with a diameter of ~120 nm and a height of ~70 nm. It is anchored in the membrane of the nuclear envelope by eight spokes, which according to electron microscopic studies of amphibian oocytes (Akey, 1989) causes the minimum center-to-center distance between different pores to be ~145 nm.

The nuclei of average somatic mammalian cells carry some 1000 NPCs. How NPCs are arranged in the nuclear envelope and whether the arrangement has a functional significance are essentially unknown. In his comprehensive review on the NPC, Maul (1977) stated that a "random distribution has never been proved, and all investigated cases seem to have non-random distribution." In fact, there are also a few examples of specialized cells, such as certain spores, in which NPCs occur in linear or orthogonal arrays. Furthermore, recent hypotheses on the coupling of gene activity and nucleo-cytoplasmic transport (Blobel, 1985) or the organization of interphase chromatin in chromosomal territories (Cremer et al., 1993) are compatible with a nonrandom distribution of the NPC. Recently (Doyé et al., 1994; Wente and Blobel, 1994; Pemberton et al., 1995) the mutation of certain nuclear pore proteins in yeast was observed to induce NPC clustering concomitant with RNA export defects.

In this paper we describe a fluorescence microscopic method for visualizing single NPCs and determining their relative coordinates in the nuclear envelope. The method builds on observations first made by Davis and Blobel (1986) showing that the labeling of cell nuclei with fluorescent NPC-specific antibodies results in a punctate staining of the nuclear periphery. However, the question of whether the observed fluorescent spots actually represent single NPCs or rather NPC clusters has so far remained unanswered. When we first looked at the punctate pattern by high-resolution confocal imaging of NPCs in digitonin-permeabilized 3T3 cells, we got the impression (Fig. 1) that single NPCs could be well discriminated; we decided to test this hypothesis.

Here we show by studies on a well-defined model system that the resolution of the confocal microscope is sufficient to visualize single NPC-sized particles and to distinguish between single particles and particle aggregates. In addition, by employing recently introduced algorithms for single particle localization and tracking (Barak and Webb, 1981; De Brabander et al., 1985; Anderson et al., 1992), we show that the relative position of the NPCs can be determined with a lateral accuracy of <20 nm and an axial accuracy of ~20 nm. Using modern statistical methods for the characterization of particle distributions (Diggle, 1983; König et

Received for publication 5 December 1995 and in final form 23 January 1996.

Address reprint requests to Dr. Reiner Peters, Institut für Medizinische Physik und Biophysik, Robert-Koch-Strasse 31, 48149 Münster, Germany. Tel.: 251-836933; Fax: 251-835121; E-mail: petersr@uni-muenster.de.

© 1996 by the Biophysical Society

0006-3495/96/05/2067/11 $2.00

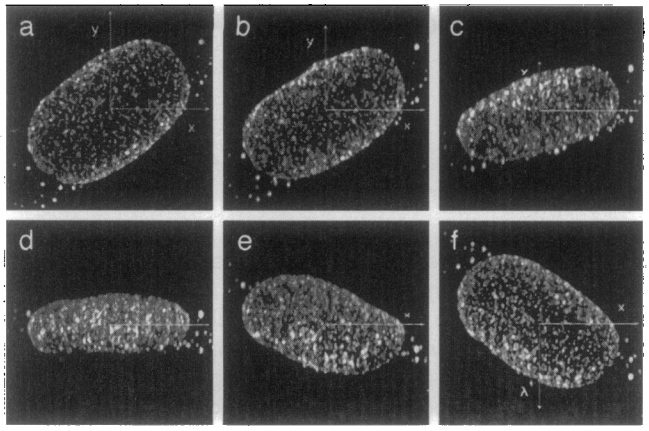

FIGURE 1 High-resolution confocal imaging and three-dimensional reconstruction of the punctate pattern seen after labeling of the nuclear periphery with an antibody specific for nuclear pore complex proteins. 3T3 cells were permeabilized by digitonin, and NPCs were labeled with mAb414 and a secondary fluorescent polyclonal antibody. Sixty optical sections of a single nucleus spanning an axial range of 12 μm were generated by confocal imaging (total image area, 25 $\times$ 25 μm^2). A three-dimensional reconstruction was performed using user written software and National Institutes of Health-Image (Rasband and Bright, 1995). The reconstruction was then rotated in steps of 30°, as shown in *a* to *f* around the *x* axis.

al., 1989; Kubitscheck et al., 1993), we demonstrate how an experimentally determined distribution can be analyzed for randomness and pattern formation. We apply the new method to digitonin-permeabilized 3T3 cells and analyze parts of the nuclear periphery of eight individual nuclei. For these the statistical analysis clearly showed that the NPCs were distributed at random. The minimum center-to-center distance between NPCs was found to be 138 $\pm$ 17 nm, in excellent agreement with earlier and more recent (early works reviewed by Maul, 1977; Akey, 1989; Oberleithner et al., 1994) electron and atomic force microscopic determinations.

The new method also has implications for topics other than the NPC distribution. In the Discussion we will consider whether the method can be used for directly observing the transport of single particles and molecules through individual NPCs.

MATERIALS AND METHODS

Antibodies

The monoclonal antibody mAb 414, which has a rather broad specificity for several nucleoporins of the p62 class, was obtained from Babco (Berkeley Antibody Company, Richmond, CA). The polyclonal sheep anti-mouse IgG-fluorescein isothiocyanate (F3008; Sigma-Aldrich Vertriebs-GmbH, Deisenhofen, Germany) was used as a secondary antibody in a two-step labeling procedure.

Cells and NPC labeling

3T3 cells were cultured in Dulbecco's modified Eagle's complete medium (Boehringer Mannheim, Germany) at 37°C in 5% CO_2 and passaged every 3 days. For labeling, cells were used 24–48 h after seeding on coverslips. Cells were permeabilized with digitonin according to the method of Adam et al. (1990), incubated with the primary antibody mAb 414, diluted 1:3000 in phosphate-buffered saline (PBS) supplemented with 1% bovine serum albumin (BSA) (PBS-BSA, pH 7.4) for 30 min, washed three times in PBS-BSA, and incubated with the secondary polyclonal antibody F3008 (diluted 1:100 in PBS-BSA for 30 min). All labeling steps were performed at 4°C. After washing, coverslips were mounted upside down on glass slides, with spacers used to create a little chamber containing 5 μl mounting buffer (3$\times$ PBS-BSA mixed with 66% glycerol and containing 2.5% of the anti-fading compound Dabco; Sigma-Aldrich).

Model system preparation

Suspensions of fluorescent microbeads of 105 nm and 170 nm nominal diameter (Fluoresbrite beads; Sigma-Aldrich) were sprayed (Micro-Spray; Agar Aids, Stansted, England) onto standard electron microscopic copper finder grids covered with a pioloform membrane of 100–200 nm thickness. The beads were primarily deposited in droplets, which rapidly dried to leave behind circular areas crowded with microbeads. By an appropriate dilution of the bead suspension the average density of beads in the circular areas was adjusted to ~5/μm^2, mimicking the density of NPCs in the nuclear envelope of 3T3 cells. For confocal laser scanning microscopy the grids were placed on a glass slide with the pioloform layer carrying the beads on top, embedded in mounting buffer, and covered with a coverslip.

Electron microscopy

For electron microscopy of samples inspected previously by confocal microscopy the electron microscopy finder grids had to be recovered from the glass slides. The coverslips were carefully lifted by the addition of a surplus of glycerine to the edges. The grid was then carefully removed with forceps, gently washed with distilled water, and dried. The grid was examined in a Hitachi H500 transmission electron microscope operated at 75 kV at a magnification of about 10,000$\times$. The magnification unit of the microscope was calibrated using latex spheres of different sizes. Photographs were taken on Agfa Gevaert 23D56 films, which were scanned into an image-processing computer for further analysis.

Confocal microscopy of cell and microbead samples

Specimens containing cells with fluorescently labeled NPCs or microbeads were imaged with a confocal laser scanning microscope (TCS; Leica, Heidelberg, Germany). Fluorescence was excited with the 488 nm line of an air-cooled Ar^+ laser and measured beyond 510 nm. Data acquisition conditions were carefully optimized by using eightfold line averaging, oil immersion objectives (63$\times$, NA 1.4, and 100$\times$, NA 1.3), lateral scanning areas of 20 $\times$ 20 μm^2 (corresponding to ~40 nm/pixel), axial steps of 0.2 μm, and a small pinhole size. Bead samples were very even, and only six planes were imaged. In the case of nuclei, stacks comprising 11–16 images were acquired, thus comprising an upper spherical shell of the cell nucleus.

The optical resolution of our confocal microscope was determined by imaging 30-nm gold beads immobilized in a 30% polyacrylamide gel. At the instrumental settings described above the full-width half-maximum (FWHM) of the images of the gold beads was found to be 0.19 μm in the lateral direction and 0.5 μm in the axial direction. Because NPCs as well as the employed beads had diameters slightly below optical resolution, their actual structures could not be resolved. Nevertheless, both NPCs and beads could be detected as bright diffraction-limited spots. In cases in which the center-to-center distances between NPCs or particles was close to or below optical resolution, the diffraction-limited spots overlapped. However, because the resultant spots no longer were circular but rather were elongated or elliptical, their composition of two or more single-particle spots could still be recognized.

Image processing and analysis

Before analysis image stacks were corrected for a small amount of photobleaching that inevitably occurred during data acquisition (~1% per image). Then the image stacks were smoothed with a 3 × 3 × 3 gaussian kernel. For determination of the center locations of the diffraction-limited three-dimensional (3D) intensity distributions, an interactive image processing computer program was developed. Small 3D analysis cubes could be selected within the image stack. These cubes defined the respective regions of interest (ROIs) to reduce computation time requirements.

The localization was performed in three steps. First, only spots were considered that were well separated from other spots and apparently derived from single NPCs/beads. For these spots the 3D intensity distribution was fitted to a 3D gaussian by minimizing the χ^2 function with a Levenberg-Marquardt routine (Press et al., 1992) to determine the axial and lateral standard deviations and offset levels. These parameters were individually determined for each image stack, because they depended on acquisition conditions such as depth in the sample and background level. In a second step all ROIs containing single spots were selected, and the centers and amplitudes of the respective spots were automatically determined by a fit to a 3D gaussian utilizing the determined SD and offset level. This resulted not only in a coordinate list of the spot centers, but also in minimum and maximum values for single spot intensities. These values were used as restrictions in the further analysis. In a third step, intensity distributions presumably comprising two or more NPCs/beads were evaluated individually. The analysis ROI was selected, and the putative centers of NPCs/beads were selected interactively by clicking with the mouse onto respective ROI voxels. The position and intensity values of these voxels served as starting values for the fitting procedure that simultaneously used up to six 3D gaussians to reproduce the ROI intensity distribution optimally, and thus to locate the centers of NPCs/beads. After convergence of the Levenberg-Marquardt routine, the analysis program inverted the voxel values nearest to the centers such that three-dimensional crosses indicating the detected NPC/bead centers were created in the image stack. In this way the fitting results could be shown without loosing the original data. After each fitting process the results were checked by inspecting an image stack composed of the original data, the fitted intensities, and the absolute residuals. In case of an unsatisfying fitting result, the voxel values of the marker crosses were inverted once more to reproduce the original intensity data, and the process started once more after the selection of new start values.

In the case of nuclei the outcome of the complete analysis was a list of the x, y, and z coordinates of 300 to 500 spots located on the upper spherical shell of the cell nucleus, assumed to represent the positions of single NPCs.

Statistical analysis

Procedures for the analysis of object patterns in two or three dimensions have recently been discussed in some detail (Diggle, 1983; König et al., 1990; Karlsson and Liljeborg, 1994). The procedures applied in this study are therefore somewhat standard and will be only briefly summarized. Estimators for the nearest-neighbor distribution function $d(r)$ and the pair correlation function $g(r)$ were used according to the methods of König et al. (1990) and Karlsson and Liljeborg (1994). Standard techniques (Diggle, 1983; Karlsson and Liljeborg, 1994) were also employed to deal with edge effects in finite samples.

Before the computation of distribution functions the experimentally determined ensembles of cartesian coordinates, each representing the locations of NPCs in the imaged portion of a particular nucleus, were transformed into spherical coordinates. Each set of cartesian coordinates defined a surface, namely a relatively small part of the upper periphery of the nucleus. By fitting procedures we found that the real surface could be well approximated by a spherical calotte. Projection of the cartesian NPC coordinates onto the best-fitting calotte resulted in a new set of corrected spherical coordinates. These were used to unambiguously determine the distance between NPCs as the arc length. For comparison, the distribution functions were also calculated for truly random distributions. For that purpose ensembles of particle coordinates were generated using a random number generator (Press et al., 1992). These particles were sequentially deposited on a spherical surface, accounting for particle impermeability by rejecting particles whose next-neighbor distance was equal to or smaller than the assumed particle diameter.

Nearest-neighbor distribution function

This function, $d(r)$, is computed in principle by measuring the nearest-neighbor distance for each particle of an ensemble and then plotting the accumulated frequency of the nearest-neighbor distances versus distance. Explicitly,

$$\mathrm{d}(r) = P(\text{distance from a typical point of the nearest point of the process is at most } r), \quad (1)$$

where P is the accumulated probability. For the stationary Poisson point process, that can be used as a model for complete spatial randomness,

$$\mathrm{d}_{\mathrm{Poi}}(r) = 1 - \exp(-\pi r^2 \rho), \quad (2)$$

where ρ denotes the average surface density of objects. Thus, object aggregation is indicated by an excess of short nearest-neighbor distances compared to the Poisson reference model, whereas a lack of nearest-neighbor distances indicates either a finite diameter of the objects and/or some repulsive interaction between them.

Pair correlation function

The distance distribution of objects is determined by their pair correlation function, $g(r)$ (McQuarrie, 1976). Choosing a typical central object, the average number of objects $n(r)\,\mathrm{d}r$ located in a shell of radii r and $r + \mathrm{d}r$ is given by

$$n(r)\mathrm{d}r = \rho g(r) 2\pi r\,\mathrm{d}r. \quad (3)$$

Thus, the pair correlation function $g(r)$ describes deviations from the average density of the local density in a ring r, $r + \mathrm{d}r$ around a typical object. For Poisson distributed point objects, $g_{\mathrm{Poi}}(r) = 1$ for $r > 0$, because there are on average no deviations between local and global density.

Cluster analysis

A cluster analysis according to Schwarz and Exner (1983) was performed for all coordinate ensembles. For a random distribution of particles the ratios of the expected mean value of the nearest-neighbor distances $E(d_{\mathrm{nn}})$ to the sample mean $\langle d_{\mathrm{nn}} \rangle$, and of the expected variance $E(s)$ to the sample variance s should be unity. Deviations of these ratios to values below or above unity indicate aggregation or repulsion between the particles.

RESULTS

Test of experimental and statistical methods using a model system

Droplets of a suspension of fluorescent microbeads with nominal diameters of 105 nm or 170 nm were deposited on electron microscopic finder grids and dried, as described in Materials and Methods. By dilution of the bead suspension the average density of beads in the dried droplets was adjusted to that of NPCs in the nuclear envelope, namely 4–5/μm^2. The samples were first imaged by fluorescence

confocal microscopy and then by transmission electron microscopy. In the electron microscope the very same sample regions studied before by confocal microscopy were located and imaged at a resolution of better than 1 nm.

An example is shown in Fig. 2. Here, 105-nm beads were imaged by confocal (Fig. 2 *a*) and electron (Fig. 2 *b*) microscopy. The confocal image is an average of six axial sections, combining the axial information for direct comparison with the transmission electron microscope (TEM) image. A good correspondence between both images is obvious. However, several bead doublets or triplets were mistakenly taken for single beads in the confocal laser scanning microscope (CLSM) image analysis. This was not surprising, because many beads were smaller than the nominal value of 105 nm, thus exceeding the capabilities of our methods. In samples containing 170-nm beads, on the other hand, doublets and triplets could easily be recognized (data not shown). The generally good correspondence between light and electron microscopic imaging is seen more clearly in Fig. 2 *c*, in which small corresponding areas of Fig. 2, *a* and *b* (boxes), were enlarged and superimposed. Magnification and overlay of larger areas revealed small deviations, probably due to local heating and a following distortion of the pioloform layer in the TEM. When samples containing 170-nm beads were imaged in the same manner (data not shown), the correspondence between CLSM and TEM images was even better than in the case of 105-nm beads, although some distortion of the sample was also noticed.

To assess the accuracy by which beads could be localized in a more quantitative manner, center regions of images such as those in Fig. 2 were analyzed in detail. The centers of the microbeads were located by the interactive procedure described in Materials and Methods for both the confocal and the corresponding electron microscopic images. This yielded two sets of coordinates, $\{\mathbf{r}_{i,CLSM}\}$ and $\{\mathbf{r}_{i,TEM}\}$, where i designates the particle number. Because all single beads were clearly resolved in the TEM images, the particle centers determined from these were assumed to be the true locations with an error of a few nanometers only. The positional lateral error made by confocal microscopy could thus be easily determined and was found to be 17 nm for 105 nm beads. We assume that the true error is even smaller, because the thus determined value probably includes some deviation caused by physical distortion of the pioloform layer in the electron microscope. The axial error was estimated by comparing the axial positions of several

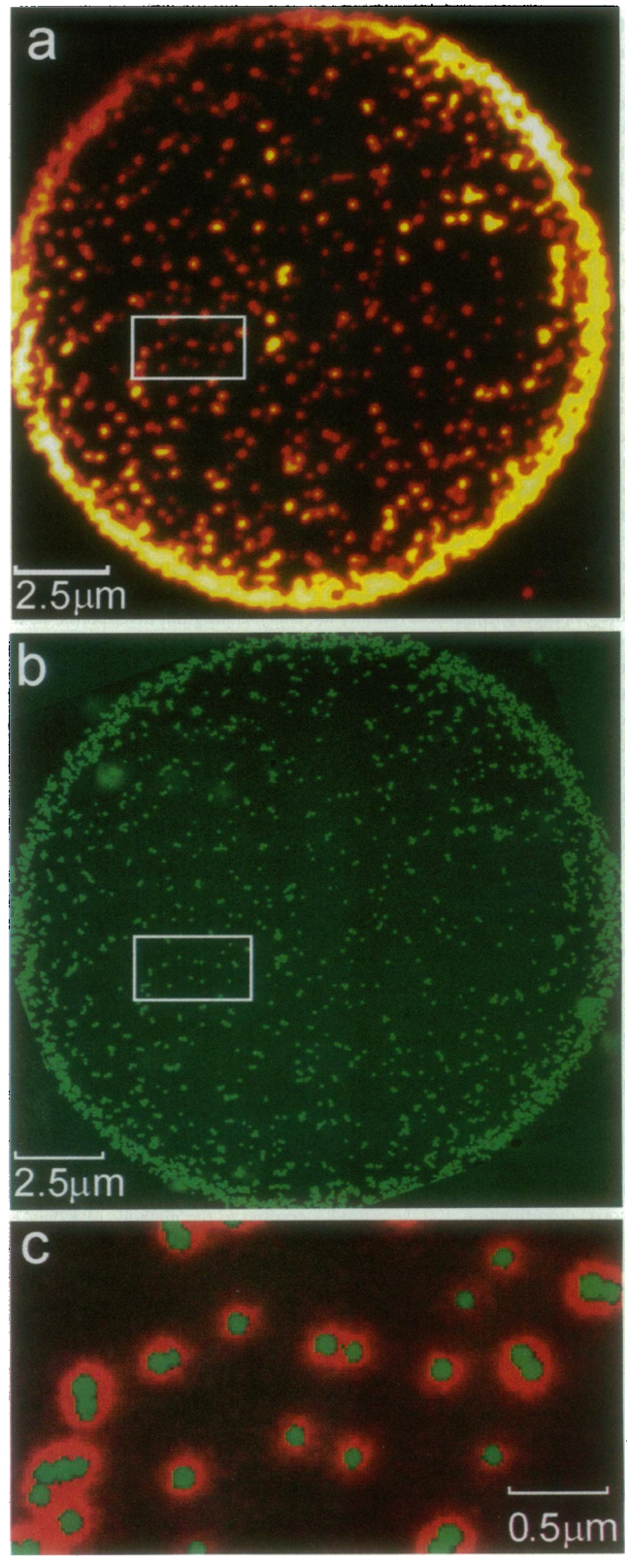

FIGURE 2 Comparative confocal and electron microscopy of identical sample areas containing fluorescent microbeads with a diameter of 105 nm. (*a*) Beads were attached to the pioloform layer of an electron microscopic finder grid, immersed in glycerol, and viewed through a microscopic coverslip in fluorescence mode. After confocal imaging, six confocal sections were combined to produce this extended focus image of the bead sample. (*b*) The very same sample area as seen by transmission electron microscopy. All microbeads were clearly resolved. A comparison between the two images shows a very good correspondence. (*c*) Overlay of a small region of the confocal and electron microscopic images (marked with a white rectangle in *a* and *b*). This direct comparison shows the good agreement between the two images. Single beads were clearly observable with the confocal microscope. Overlay of larger areas revealed small systematic deviations, probably due to heating and distortion of the pioloform layer in the TEM.

closely neighboring single beads, assuming their axial positions were identical within a few nanometers, because they were attached to the nearly planar pioloform layer. The corresponding axial positions agreed with each other within an error of 20 nm.

The quantitative analysis was carried further by calculating the nearest-neighbor distribution function $d(r)$ and the pair correlation function $g(r)$ for the experimentally obtained coordinate sets $\{\mathbf{r}_{i,CLSM}\}$ and $\{\mathbf{r}_{i,TEM}\}$, as well as for simulated random distributions. For the latter, $d(r)$ and $g(r)$ were first calculated for 100 individually simulated random distributions $\{\mathbf{r}_i\}_j$, $j = 1, 2, \ldots, n$, of hard core particles, employing diameters and area densities corresponding to those of the microbead samples. The outcome of individual simulations was then averaged to obtain a reliable reference. The results of all these calculations are given in Fig. 3.

Fig. 3 allows several interesting conclusions to be drawn. Both distribution functions, $d(r)$ (Fig. 3 *a*) and $g(r)$ (Fig. 3 *b*), calculated from confocal data ($\{r_{i,CLSM}\}$, *filled circles*) and electron microscopic data ($\{r_{i,TEM}\}$, *open circles*) unequivocally indicated an average minimum particle diameter of ~100 nm; no nearest-neighbor distances of <90 nm were detected. This was not surprising for the TEM data. Remarkably, however, the CLSM data yielded the same value, although the optical resolution was ~270 nm (lateral FWHM of single beads). Thus, it was possible not only to locate particles with an accuracy well below the optical resolution limit, but also, by combining numerical image processing with statistical nearest-neighbor analysis, to deduce the particle diameter. In fact, to our best knowledge, our data represent the first demonstration that the size of particles as small as 105 nm can be accurately determined by light microscopy.

A close inspection of the micrographs in Fig. 2 clearly shows that microbeads were heavily aggregated. This is also demonstrated by the distribution functions $d(r)$ and $g(r)$ by the large deviations from the randomly distributed hard core particles. The clustering is shown in a particularly impressive manner by the pair correlation functions $g(r)$ (Fig. 3 *b*): the functions pertaining to experimental data have marked maxima at distances just larger than the particle diameter. Aggregation was detected by the pair correlation functions of both CLSM and TEM data. This is quite remarkable because confocal imaging sometimes missed particularly small or closely spaced particles, as mentioned above. These missed closely spaced particles cause the difference in the result for $d(r = 105$ nm) between the CLSM and TEM data sets. The CLSM distribution function value reaches 57% of the TEM value (Fig. 3 *a*). This was significantly improved for the 170-nm beads, where the CLSM values for $d(r = 170$ nm) reached 90% of the TEM value (data not shown).

A cluster analysis (Table 1) according to Schwarz and Exner (1983) supported the above conclusion that the microbeads were heavily aggregated. The averaged nearest-neighbor distances between the microbeads $\langle d_{nn}\rangle$ and their respective variances s were calculated from CLSM and

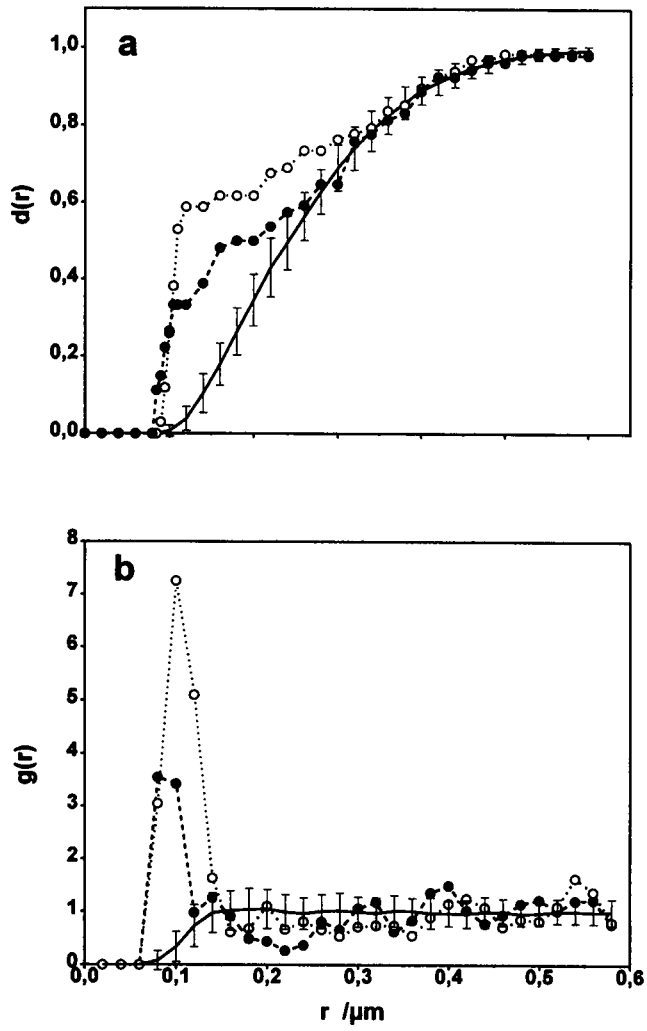

FIGURE 3 Distribution functions of the model microbead system as shown in Fig. 2. (*a*) Nearest-neighbor distribution functions $d(r)$ were calculated from the bead positions $\{r_{i,CLSM}\}$ and $\{r_{i,TEM}\}$ that were determined from the CLSM (●) and TEM (○) images shown in Fig. 2, respectively, as described in Materials and Methods. The full line corresponds to the averaged nearest-neighbor distribution function of simulated random disks with an average particle diameter of 105 nm. (*b*) Pair correlation functions $g(r)$ calculated from $\{r_{i,CLSM}\}$ (●) and $\{r_{i,TEM}\}$ (○). The full line corresponds to the averaged pair correlation function of the random disks. For the latter, $d(r)$ and $g(r)$ were first calculated for 100 individually simulated random distributions of hard core particles, employing a diameter distribution and area density corresponding to those of the microbead sample. The averaged outcome of individual simulations is shown with the corresponding SD. Both $d(r)$ and $g(r)$ calculated from confocal and electron microscopic data indicated an average minimum particle diameter of ~100 nm; no nearest-neighbor distances of <90 nm were detected. The large deviations from the randomly distributed hard core particles indicate a strong particle aggregation, as can be noted in Fig. 2.

TEM data, and expectation values for the nearest-neighbor distance $E(d_{nn})$ and the corresponding variances $E(s)$ were determined from the random particle distributions ($d = 105$ nm). The ratio values $\langle d_{nn}\rangle/E(d_{nn})$ and $s/E(s)$ were determined as 0.76 and 1.65 for the CLSM data, and as 0.72 and 1.21 for the TEM data, respectively. In both cases $\langle d_{nn}\rangle/$

TABLE 1 Cluster analysis of microbead and NPC data

	Experimental data		Random points		Random disks		Ratios			
Data set	$\langle d_{nn} \rangle$ (μm)	s (μm^2)	$E(d_{nn})$* (μm)	$E(s)$‡ (μm^2)	$E_s(d_{nn})$* (μm^2)	$E_s(s)$‡ (μm^2)	$\frac{\langle d_{nn} \rangle}{E(r)}$	$\frac{s}{E(s)}$	$\frac{\langle d_{nn} \rangle}{E_s(d_{nn})}$	$\frac{s}{E_s(s)}$
Beads CLSM	0.266	0.029	—	—	0.348	0.010	—	—	0.76	1.65
Beads TEM	0.204	0.020	—	—	0.144	0.014	—	—	0.73	1.21
Nuclei										
a	0.286	0.010	0.239	0.015	0.280	0.010	1.19	0.681	1.02	1.02
b	0.275	0.008	0.226	0.014	0.270	0.009	1.22	0.590	1.02	0.87
c	0.286	0.014	0.254	0.017	0.297	0.013	1.09	0.84	0.93	1.13
d	0.288	0.015	0.262	0.019	0.304	0.014	1.10	0.78	0.95	1.06
e	0.315	0.011	0.252	0.017	0.292	0.001	1.25	0.63	1.01	1.04
f	0.267	0.012	0.223	0.013	0.268	0.011	1.20	0.87	1.00	1.32
g	0.298	0.016	0.258	0.018	0.300	0.013	1.16	0.91	1.00	1.24
h	0.269	0.013	0.231	0.014	0.275	0.009	1.16	0.89	0.98	1.43
Mean	0.285	0.012	0.243	0.016	0.286	0.010	1.17	0.77	0.99	1.14
SD	0.016	0.003	0.015	0.002	0.014	0.004	0.055	0.12	0.03	0.18

*$E(d_{nn})$; expected mean of the nearest-neighbor distance for random particle distributions. For points this was calculated according to equation 4 from Schwarz and Exner (1983), and for hard core particles of diameter d it was calculated from N simulated random distributions (N = 100, d = 105 nm for microbead analysis, and N = 1000, d = 145 nm for NPC analysis).

‡$E(s)$; expected variance of the nearest-neighbor distance for random distributions. For point particles it was calculated according to equation 5 from Schwarz and Exner (1983), and for hard core particles it was determined from simulated random distributions (see above).

$E(d_{nn})$ ratios were smaller than unity, whereas $s/E(s)$ ratios were larger than unity. This is indicative for clustered sets of particles with a superimposed randomly distributed background (Schwarz and Exner, 1983). Again, results from the analysis of CLSM and TEM data were comparable on a qualitative basis.

Distribution of nuclear pore complexes in the nuclear envelope of 3T3 cells

NPC labeling

Monolayers of 3T3 cells were permeabilized by treatment with digitonin, and the NPC was labeled with the anti-nucleoporin antibody mAb 414 and a fluorescent secondary antibody. Cell nuclei exhibited the characteristic punctate pattern typical for NPC staining. Interestingly, a few bright spots were frequently seen in the cytoplasm, possibly pertaining to annulate lamellae. Control experiments in which a first antibody of irrelevant specificity was used, or the first mAb was omitted, showed no staining above a small autofluorescence background level (data not shown).

NPC localization

Stacks of high-resolution confocal images (Fig. 4 *a*) were acquired from selected nuclei. Usually only the top region of a nucleus was imaged by 11 to 16 confocal sections with an axial step size of 0.2 μm. Before any further analysis, the images were corrected for photobleaching and smoothed. The images showed a multitude of fluorescent spots, among which two populations could be discriminated. One consisted of small diffraction-limited spots with radially symmetric intensity profiles corresponding to the optical resolution (Table 2). Thirty to seventy such spots occurred per image stack. The other population consisted of clusters of small diffraction-limited spots. Of these about 90–180 occurred per image stack. We assumed that the small spots represented single NPCs, whereas the clusters represented NPC separated from each other by distances smaller than the optical resolution limit.

The three-dimensional intensity distributions of the fluorescent spots were fitted by 3D gaussians, employing a single gaussian in the case of small spots and up to six gaussians simultaneously in case of clusters (cf. Materals and Methods). The quality of the fitting processes was assessed by the value of the χ^2 function, by the visual correspondence between the data and the results of the fitting process, and by a three-dimensional graphical representation of the absolute residuals as shown in Fig. 4 *c*. In the upper trace of Fig. 4 *c* the selected analysis cube is shown, with seven crosses marking the positions of found NPC centers. The middle trace shows the result of the fitting process. In this case the overlapping intensity distributions of six NPCs have been reproduced in a seemingly perfect way. The center of the NPC in the upper right-hand corner of the data trace was determined in the second step of the analysis, as described in Materials and Methods; therefore it does not show up in this simulated image stack. The lower trace shows the absolute difference between the data and the fitting outcome. The small deviations from zero intensity values for the six fitted NPCs are due to the data noise.

The image analysis resulted in a data table containing the spot center coordinates and the intensity values of all spots in the analysis region. From these data the complete image

stack could be reproduced, proving that the fitting process allowed a very close representation of the original data. This is shown in Fig. 4 *b*. Eight different 3T3 cells with 300 to 400 spots in the upper spherical segment of the nuclei were analyzed in this way. The acquired coordinate values were corrected by projection onto a best-fitting spherical surface.

Distribution functions

For each nucleus the nearest-neighbor distribution and pair correlation functions were calculated for the spot centers located in a circular region with a radius of 3 to 5 μm on the top of the nucleus. Table 2 gives the radii of the respective circular analysis regions, the number of spots evaluated in this area, and their surface density. For each of these different surface densities, we simulated 1000 random distributions of hard core particles with a diameter of 145 nm by a Monte Carlo simulation program. The distance distribution functions were computed for each of the random particle ensembles. The results for respective distances were averaged, and the standard deviations were determined.

Fig. 5 shows the nearest-neighbor distribution functions of eight nuclei (*filled circles*), together with the functions of the randomly distributed hard core particles (*solid line*, bars correspond to SD). In addition, the analytical result according to Eq. 2 for point particles is shown (*dashed line*). Obviously, the nearest-neighbor distribution functions of the spots did not agree with the function for point particles. The data complied much better with the results of the hard core particle distributions. As Fig. 5 shows, extrapolation of the downward slope of the curves for the hard core particles pointed to the particle diameter, because it represented the lower limit for nearest-neighbor distances, d_{nn}. The extrapolation yielded a value of $d_{nn,ave} = 138 \pm 17$ nm for the curves determined from the image data. This value is in good agreement with the results of recent electron micro-

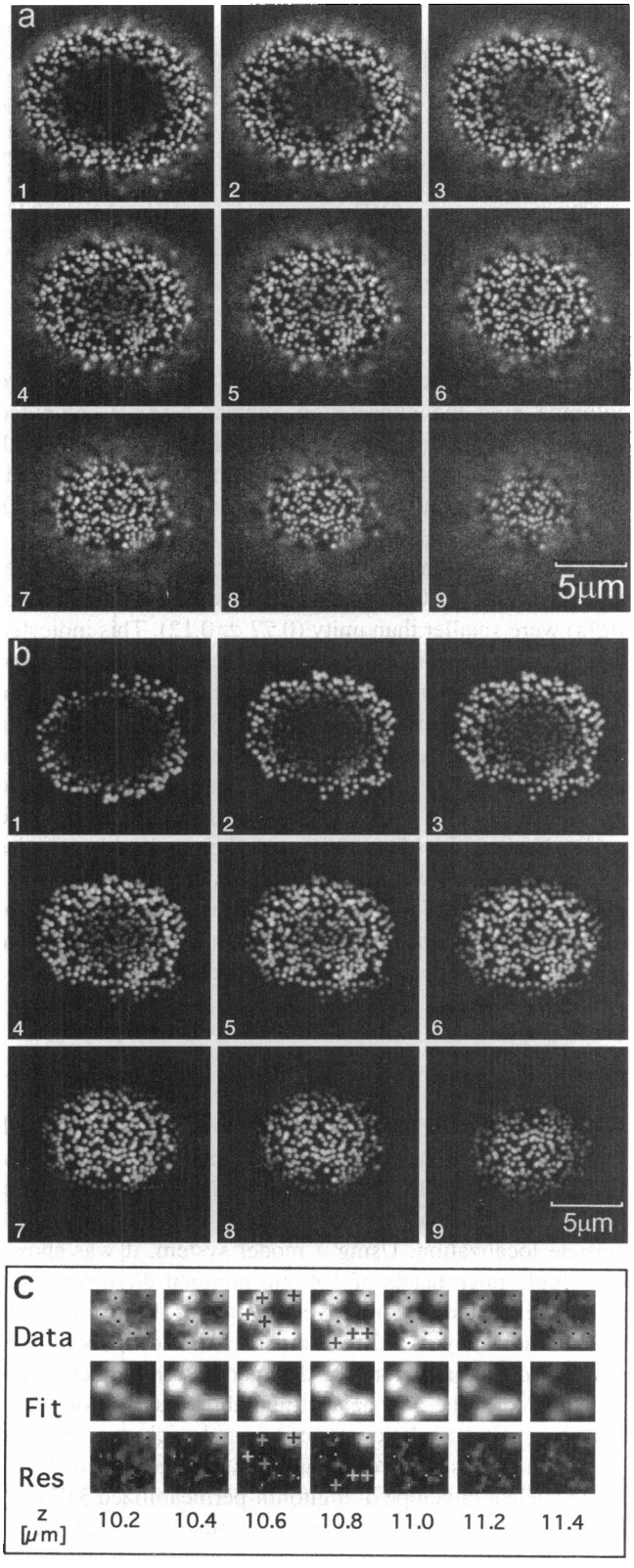

FIGURE 4 Confocal imaging and 3D localization of NPCs. (*a*) 3T3 cells were permeabilized with digitonin, and nuclear pore complexes were fluorescently labeled with the anti-nucleoporin antibody mAb414. Nine of 11 confocal sections (axial step size 0.2 μm) from a single cell nucleus are shown. The images were corrected for photobleaching and smoothed by a $3 \times 3 \times 3$ gaussian kernel. Many diffraction-limited spots and clusters of diffraction-limited spots can be detected. Presumably the small spots represent single NPCs, whereas the clusters represent NPCs separated from each other by distances smaller than the optical resolution limit. (*b*) Reconstruction of the original image intensity distribution by the result of the fitting process utilizing the determined NPC locations and intensities. The three-dimensional intensity distributions of the fluorescent spots were fitted by 3D gaussians, employing a single gaussian in the case of small spots and up to six gaussians simultaneously in the case of clusters (cf. Materals and Methods). (*c*) Data analysis cube, fitting outcome, and absolute difference image. The quality of the fitting processes was assessed for each analysis cube by the visual correspondence between data (*first row*), results of the fitting process (*second row*), and the graphical representation of the absolute residuals (*third row*). In the first image row seven 3D crosses mark the voxels that correspond most closely to the positions of found NPC centers. The z planes where the NPC centers were located are marked with 2D crosses. Planes above and below the xy position are indicated by a dot. The center of the NPC in the upper right-hand corner of the data trace was determined beforehand; therefore it was not simulated in the fitted image stack. Here the overlapping intensity distributions of six NPCs were perfectly reproduced, as can be judged by the very low intensity values in the difference image trace.

TABLE 2 Statistical data of the eight 3T3 cell nuclei for which distribution functions were calculated and cluster analysis performed

Nucleus	No. of NPCs in analysis region	Radius of analysis region (μm)	Radius of the best-fitting sphere (μm)	FWHM of diffraction-limited spot (radial) (μm)	FWHM of diffraction-limited spot (axial) (μm)	Surface density of NPCs in analysis region (μm^{-2})	d_{crit}* (μm)
a	222	4.0	13.2	0.322	0.940	4.4	0.157
b	177	3.4	14.2	0.302	0.974	4.9	0.142
c	143	3.4	12.5	0.262	0.873	3.9	0.118
d	165	3.8	16.6	0.255	0.907	3.6	0.125
e	342	5.3	15.7	0.242	0.873	3.9	0.169
f	149	3.1	11.3	0.242	0.873	5.0	0.140
g	187	4.0	11.7	0.269	0.940	3.8	0.128
h	189	3.6	10.2	0.269	0.940	4.7	0.125
Mean	196.7	3.8	13.2	0.270	0.923	4.3	0.138
SD	63.8	0.67	2.2	0.028	0.03	0.5	0.017

d_{crit}*, minimum center-to-center distance of nuclear pore complexes.

scopic work (Akey, 1989) and with in vivo atomic force microscopic measurements of inter-NPC distances (Oberleithner et al., 1995). Thus, the determined particle diameter strongly supported the assumption that the diffraction-limited spots indeed represented single NPCs. Only very few particles exhibited nearest-neighbor distances below $d_{nn,ave}$. We attributed the occurrence of these smaller distances to inaccuracies in the localization process due to noisy data, or to some errors in estimating the correct numbers of pores in larger NPC patches.

Fig. 6 shows the pair correlation functions for the eight nuclei (*filled squares*) and for the simulated random distributions of hard discs (*solid lines*; bars correspond to SD). It was not necessary to calculate the pair correlation function for point objects $g_{Poi}(r)$, because it is simply unity for $r > 0$. Most of the pair correlation functions of nuclei were significantly smaller than unity for distances below 145 nm, thus not complying with randomly distributed point objects. At larger distances the pair correlation functions of nuclei approached those of randomly distributed hard spheres. The large data noise is due to the fact that $g(r)$ is calculated by taking the derivative of the numerically determined K function, which represents the normalized, accumulated mean number of particles within a given distance from typical particles (Karlsson and Liljeborg, 1994). The noise of the K function of samples with a relatively small number of particles (Table 2) appears amplified in the derivative, $g(r)$. Altogether, the data supported the conclusions drawn from the analysis of nearest-neighbor distribution functions.

Cluster analysis

Results of a cluster analysis according to Schwarz and Exner (1983) are given in Table 1 for each of the eight nuclei. In the first data column the averaged nearest-neighbor distance, $\langle d_{nn} \rangle$, of NPCs is given, followed by their variances. The next two columns give the expected nearest-neighbor distances, $E(d_{nn})$, and their variances, $E(s)$, for random point distributions calculated according to equations 4 and 5 of Schwarz and Exner (1983). The next two columns give the expectation values, $E_s(d_{nn})$, computed from 1000 simulated random distributions of particles with a diameter $d = 145$ nm, together with the respective variances. The last four columns give the ratios $\langle d_{nn} \rangle / E(d_{nn})$, $s/E(s)$, $\langle d_{nn} \rangle / E_s(d_{nn})$, and $s/E_s(s)$.

Table 1 shows that all values for $\langle d_{nn} \rangle / E(d_{nn})$ were larger than unity (1.17 ± 0.06, mean $\pm$ SD), whereas all values for $s/E(s)$ were smaller than unity (0.77 ± 0.12). This indicated that the spots exhibited a more repulsive behavior compared to randomly distributed point particles. Such effects might be due to a repulsive interaction potential or simply to a finite diameter. The latter possibility was supported by the fact that the value for $\langle d_{nn} \rangle / E_s(d_{nn})$ was 0.99 ± 0.03, and that for $s/E_s(s)$ was 1.14 ± 0.2, i.e., both being very close to unity. Hence, the distribution of the analyzed particles agreed very well with that of randomly distributed disks with a diameter of 145 nm. There were no indications of regular arrangements or aggregation of NPCs, as can be seen from the average values of the latter ratios.

DISCUSSION

The paper describes a light microscopic method by which single NPCs can be visualized and their 3D arrangement assessed. The method combines high-resolution confocal fluorescence microscopy with image analysis and single particle localization. Using a model system, it was shown that single microbeads of 105 nm nominal diameter could be visualized and their relative coordinates determined with a lateral accuracy of <20 nm and an axial accuracy of ~20 nm. Particle aggregation was detected by three independent statistical criteria: the nearest-neighbor distribution function, the pair correlation function, and a cluster analysis. The method was applied to study the arrangement of NPCs in the nuclear envelope of digitonin-permeabilized 3T3 cells labeled with an anti-nucleoporin antibody. Image stacks were obtained comprising the upper calottes of eight indi-

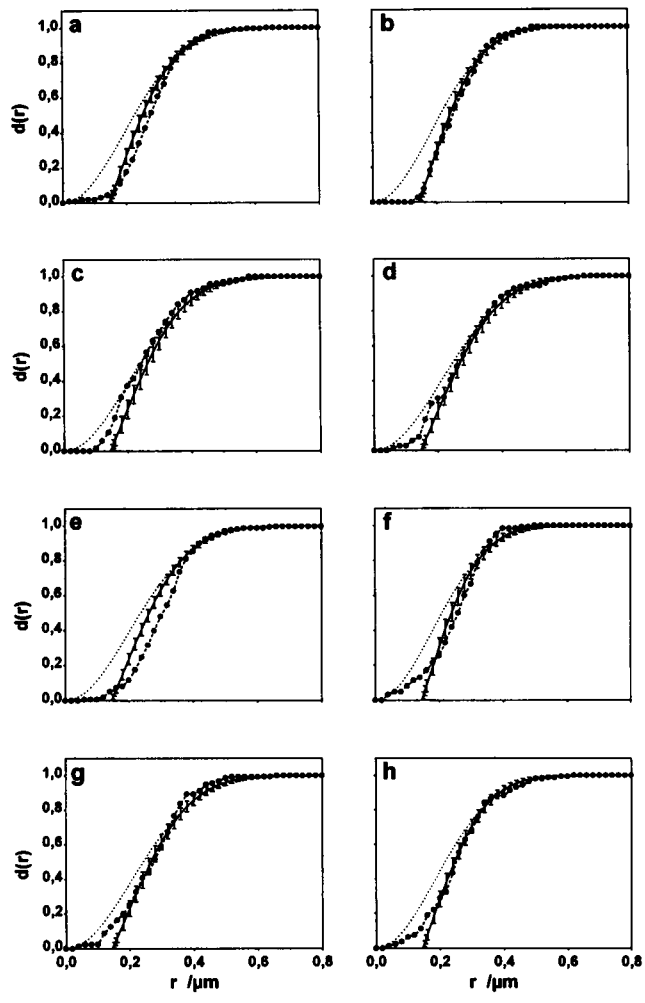

FIGURE 5 Nearest-neighbor distribution functions $d(r)$ of NPCs of single 3T3 cell nuclei. The data were calculated for NPCs from eight nuclei (a–h, ●) and are shown together with the averaged functions of randomly distributed hard core particles (*solid line*). The analytical result for point particles according to Eq. 2 is also shown (*dashed line*). For the hard core particles, $d(r)$ and $g(r)$ (see Fig. 6) were calculated for 1000 individually simulated random distributions of particles (diameter 145 nm) with area densities corresponding to those of the respective NPC data sets. The averaged outcome of the individual simulations is shown (*solid line*) with the corresponding SD. The NPC data do not agree with the function for point particles. They agree much better with the results of the hard core particle distributions. Extrapolation of the downward slope of the curves for the hard core particles indicates the average particle diameter, $d_{nn,ave}$. This extrapolation yielded $d_{nn,ave} = 138 \pm 17$ nm for the curves determined from the image data. This particle diameter strongly supported the assumption that the diffraction-limited spots indeed represented single NPCs. Only very few spots displayed nearest-neighbor distances below $d_{nn,ave}$. The occurrence of these smaller distances was probably due to inaccuracies in the localization process due to noisy data.

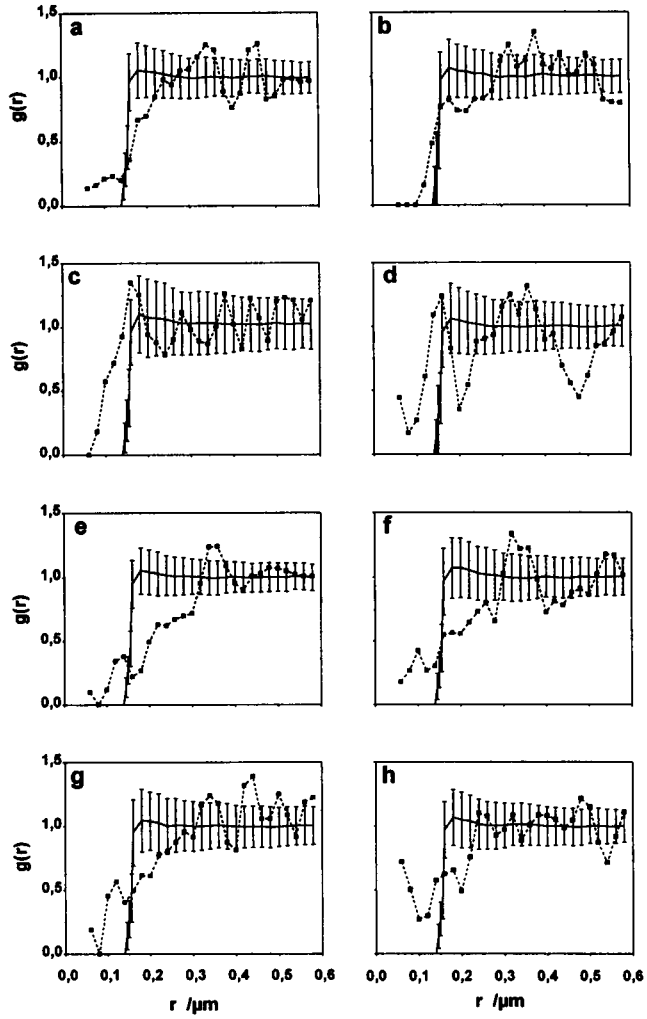

FIGURE 6 Pair correlation functions $g(r)$ of NPCs on single 3T3 cell nuclei. The pair correlation functions are shown for eight nuclei (a–h, ■) and for simulated random distributions of hard core particles of appropriate densities with a diameter of 145 nm (*solid lines*; bars correspond to SDs; for details see legend of Fig. 5). $g(r)$ for point objects is unity for $r > 0$. Most of the pair correlation functions of nuclei were significantly smaller than unity for distances below 145 nm, thus not complying with randomly distributed point objects. At larger distances the pair correlation functions of nuclei approached those of randomly distributed hard spheres. Altogether, the data supported the conclusions drawn from the analysis of nearest-neighbor distribution functions.

vidual nuclei. NPCs could be visualized as bright diffraction-limited spots. Further analysis showed that the NPCs had a minimum center-to-center distance of 138 ± 17 nm and were distributed at random.

The present study was concerned with 3T3 cells, an established fibroblast cell line. The statistical analysis was based on a sample comprising eight different nuclei with a total of about 1600 NPCs. Therefore we assume that NPCs are randomly distributed in the nuclear envelope of 3T3 cells. We also speculate that the same holds in general for secondary, fast-growing, nondifferentiated cells. However, we cannot fully exclude a possible variation in the NPC distribution during the cell cycle, as has been suggested by Markovics et al. (1974) using freeze-etching electron microcopy. It also remains an open question whether NPCs are randomly distributed in the nuclear envelope of fully differentiated primary cells. It is well established by now that chromosomes, even in interphase, are arranged in a nonrandom fashion. Interphase chromosomes occupy defined territories (Agard and Sedat, 1983; Cremer et al., 1993), pos-

sibly separated by interchromatin channels serving as highways for the transport of matter and information between genes and the nuclear periphery. Consequently, one could expect that NPCs are clustered at the peripheral endings of interchromatin channels. In addition, the gene gating hypothesis (Blobel, 1985) assumes that the genome of higher eukaryotic cells is organized into a number of distinct 3D structures being induced and maintained by the nuclear periphery and in particular by the NPCs, also invoking a nonrandom distribution of NPCs. Furthermore, there are several examples for the nonrandom distribution of NPCs under special conditions. Apoptosis, for instance, is accompanied by a severe condensation of chromatin at the nuclear periphery. Concomitant with chromatin condensation, NPCs are rearranged and accumulate in chromatin-free regions of the nuclear envelope (Lazebnik et al., 1993). Recently it was observed (Wente and Blobel, 1994; Doyé et al., 1994; Pemberton et al., 1995) that disruption of the nucleoporin gene NUP113 results in clustering of NPCs and in RNA export defects. For all of these reasons it will be interesting to apply the approach of the present paper to primary differentiated and polarized cells as well as to apoptotic and genetically modified cells.

Finally, it may be noticed that the method described in this paper also has implications for topics other than NPC distribution. Thus, we suggest applying the method in suitably modified form for analyzing the transport of single particles and even single molecules through individual NPCs. Current models of nucleo-cytoplasmic transport assume that both import and export are multistep processes. For instance, protein import seems to proceed through at least six steps (for a review, see Melchior and Gerace, 1995): receptor-ligand recognition in the cytoplasm, initial binding of the transport cargo to cytoplasmic filaments of the NPC, transport of the cargo to the cytoplasmic opening of the central channel of the NPC, translocation of the cargo through the central channel, release of the cargo at the karyoplasmic opening of the central channel, and transport of the cargo on the karyoplasmic, fish-trap-like filaments. The distances involved are 50–100 nm for the cytoplasmic filaments, 70 nm for the central channel, and 50–100 nm for the karyoplasmic filaments. The cargo can have a diameter of up to 30 nm. The transition times for the different steps are absolutely unknown, but may well be on the order of one second. Thus, it appears perfectly feasible to follow the transport of large, fluorescently labeled particles such as protein-coated microbeads or ribosomal subunits through individual NPCs by the method described in this paper. In particular, if the nuclear envelope is imaged in cross section, the spatial resolution of the method (<20 nm) and its time resolution (a maximum of 10 scans/s) are apparently sufficient. Significant progress has been made recently (Schmidt et al., 1996) in the detection and tracking of single fluorophores. Therefore, it might become possible in the near future to follow not only the transport of single particles but also of single molecules through individual NPCs.

Support from the Deutsche Forschungsgemeinschaft (grant Pe 138/14-1) is gratefully acknowledged.

REFERENCES

Adam, S., R. Sterne-Marr, and L. Gerace. 1990. Nuclear protein import in permeabilized mammalian cells requires soluble cytoplasmic factors. *J. Cell Biol.* 111:807–816.

Agard, D. A., and J. W. Sedat. 1983. Three-dimensional architecture of a polytene nucleus. *Nature.* 302:676–681.

Akey, C. W. 1989. Interactions and structure of the nuclear pore complex revealed by cryo-electron microscopy. *J. Cell Biol.* 109:955–970.

Akey, C. W., and D. S. Goldfarb. 1989. Protein import through the nuclear pore complex is a multistep process. *J. Cell Biol.* 109:971–982.

Akey, C. W., and M. Radermacher. 1993. Architecture of the *Xenopus* nuclear pore complex revealed by three-dimensional cryo-electron microscopy. *J. Cell Biol.* 122:1–19.

Anderson, C. M., G. N. Georgiou, I. E. G. Morrison, G. V. W. Stevenson, and R. J. Cherry. 1992. Tracking of cell surface receptors by fluorescence digital imaging microscopy using a charge-coupled device camera. *J. Cell Sci.* 101:415–425.

Barak, L. S., and W. W. Webb. 1981. Fluorescent low density lipoprotein for observation of dynamics of individual receptor complexes on cultured human fibroblasts. *J. Cell Biol.* 90:595–604.

Blobel, G. 1985. Gene gating: a hypothesis. *Proc. Natl. Acad. Sci. USA.* 82:8527–8529.

Cremer, T., A. Kurz, R. Zirbel, S. Dietzel, B. Rinke, E. Schrock, M. R. Speicher, U. Mathieu, A. Jauch, P. Emmerich, H. Scherthan, T. Ried, C. Cremer, and P. Lichter. 1993. Role of chromosome territories in the functional compartmentalization of the cell nucleus. *Cold Spring Harb. Symp. Quant. Biol.* 58:777–792.

Davis, L., and G. Blobel. 1986. Identification and characterization of a nuclear pore complex protein. *Cell.* 45:699–709.

De Brabander, M., G. Geuens, R. Nuydens, M. Moeremans, and J. de Mey. 1985. Probing microtubule-dependent intracellular motility with nanometer particle video ultramicroscopy (nanovid ultramicroscopy). *Cytobios.* 43:273–283.

Diggle, P. J. 1983. Statistical Analysis of Spatial Point Patterns. Academic Press, London.

Doyé, V., R. Wepf, and E. C. Hurt. 1994. A novel nuclear pore protein Nup133p with distinct roles in poly(A)$^+$ RNA transport and nuclear pore distribution. *EMBO J.* 13:6062–6075.

Earnshaw, W. E. 1995. Nuclear changes in apoptosis. *Curr. Opin. Cell Biol.* 7:337–343.

Fabre, E., and E. C. Hurt. 1994. Nuclear transport. *Curr. Opin. Cell Biol.* 6:335–342.

Falcieri, E., P. Gobbi, A. Cataldi, L. Zamai, I. Faenza, and M. Vitale. 1994. Nuclear pores in the apoptotic cell. *Histochem. J.* 26:754–763.

Forbes, D. J., and A. D. Johnson. 1995. Nucleus and gene expression. *Curr. Opin. Cell Biol.* 7:299–300.

Goldberg, M. W., and T. D. Allen. 1995. Structural and functional organization of the nuclear envelope. *Curr. Opin. Cell Biol.* 7:301–309.

Grote, M., U. Kubitscheck, R. Reichelt, and R. Peters. 1995. Mapping of nucleoporins to the center of the nuclear pore complex by postembedding immunogold electron microscopy. *J. Cell Sci.* 108:2963–2972.

Hinshaw, J. E. 1994. Architecture of the nuclear pore complex and its involvement in nucleo-cytoplasmic transport. *Biochem. Pharmacol.* 47: 15–20.

Karlsson, L. M., and A. Liljeborg. 1994. Second-order stereology for pores in translucent alumina studied by confocal scanning laser microscopy. *J. Microsc.* 175:186–194.

König, D., S. Carvajal-Gonzalez, A. M. Downs, J. Vassy, and J. P. Rigaut. 1990. Modelling and analysis of 3-D arrangements of particles by point processes with examples of application to biological data obtained by confocal scanning light microscopy. *J. Microsc.* 161:405–433.

Kubitscheck, U., R. Schweitzer-Stenner, D. J. Arndt-Jovin, T. M. Jovin, and I. Pecht. 1993. Distribution of type I Fc_ϵ-receptors on the surface of mast cells probed by fluorescence resonance energy transfer. *Biophys. J.* 64:110–120.

Lazebnik, Y. A., S. Cole, C. A. Cooke, W. G. Nelson, and W. C. Earnshaw. 1993. Nuclear events in apoptosis in vitro in cell-free mitotic extracts: a model system for analysis of the active phase of apoptosis. *J. Cell Biol.* 123:7–22.

Markovics, J., L. Glass, and G. G. Maul. 1974. Pore patterns on nuclear membranes. *Exp. Cell Res.* 85:443–451.

Maul, G. G. 1977. The nuclear and the cytopolasmic pore complex: structure, dynamics, distribution, and evolution. *Int. Rev. Cytol. Suppl.* 6:76–187.

McQuarrie, D.A. 1976. Statistical Mechanics. Harper Collins Publishers, Inc., New York.

Melchior, F., and L. Gerace. 1995. Mechanisms of nuclear protein import. *Curr. Opin. Cell Biol.* 7:310–318.

Oberleithner, H., E. Brinckmann, A. Schwab, and G. Krohne. 1994. Imaging nuclear pores of aldosterone-sensitive kidney cells by atomic force microscopy. *Proc. Natl. Acad. Sci. USA.* 91:9784–9788.

Panté, N., and U. Aebi. 1994. Toward the molecular details of the nuclear pore complex. *J. Struct. Biol.* 113:179–189.

Pemberton, L. F., M. P. Rout, and G. Blobel. 1995. Disruption of the nucleoporin gene NUP133 results in clustering of nuclear pore complexes. *Proc. Natl. Acad. Sci. USA.* 92:1187–1191.

Press, W.H., S.A. Teukolsky, W.T. Vetterling, and B.P. Flannery. 1992. Numerical Recipes in C, 2nd ed. Cambridge University Press, Cambridge, England.

Rasband, W. S., and D. S. Bright. 1995. NIH image: a public domain image processing program for the Macintosh. *Microbeam Anal. Soc. J.* 4:137–149.

Reichelt, R., A. Holzenburg, E. L. Buhle, M. Jarnik, A. Engel, and U. Aebi. 1990. Correlation between structure and mass distribution of the nuclear pore complex and of distinct pore complex components. *J. Cell Biol.* 110:883–894.

Ripley, B. D. 1981. Spatial Statistics. Wiley and Sons, New York.

Schmidt, T., G. J. Schütz, W. Baumgartner, H. J. Gruber, and H. Schindler. 1996. Characterization of photophysics and mobility of single molecules in a fluid lipid membrane. *J. Phys. Chem.* In press.

Schwarz, H., and H. E. Exner. 1983. The characterization of the arrangement of feature centroids in planes and volumes. *J. Microsc.* 129: 155–169.

Wente, S. R., and G. Blobel. 1994. NUP145 encodes a novel yeast glycine-leucine-phenylalanine-glycine (GLFG) nucleoporin required for nuclear envelope structure. *J. Cell Biol.* 125:955–969.